Effect of Different Radial Inclined Angles of Self-circulation Casing Treatment on the Transonic Axial Flow Compressor Performance

H. Zhang[1], C. Zhang[1†], F. Dong[2], X. Zhong[1] and W. Chu[1]

[1] *School of Power and Energy, Northwestern Polytechnical University, Xi'an, Shaanxi, 710129, China*

[2] *Xi'an Aerospace Propulsion Institute, Xi'an, Shaanxi, 710100, China*

†*Corresponding Author Email: 2020261997@mail.nwpu.edu.cn*

ABSTRACT

Unsteady numerical simulation of single passage was carried out on NASA Rotor 35 to study the influence of the radial inclined angle of self-circulation casing treatment (SCT) on the performance and stability of a transonic compressor at 100% design speed. The radial inclined angles were set to 0°(D0), °(D30) and 60°(D60), respectively. The calculated result indicates an increase in the stall margin improvement (SMI) and the design efficiency improvement (DEI) as the radial inclined angle increases gradually. The SMI of the SCT with a 60° radial inclined angle is 12.5%, the biggest among the three SCTs, and the peak efficiency improvements (PEI) of the SCTs are almost the same. The radial inclined angle is provided with the effect of strengthening the self-circulation casing treatment effect, which further improves the stable working range of the compressor, and the efficiency loss is also lower than that of the 0° angle structure. The flow conditions inside the bleeding part can be improved by radially skewing the self-circulating structure toward the rotor rotating direction.

Keywords: Axial transonic compressor; Self-circulation casing treatment; Radial inclined angle; Stability; Performance.

NOMENCLATURE

Ca	blade tip axial chord length		PEI	Peak Efficiency Improvement
Cal	calculation			
DEI	Design Efficiency Improvement		PTS	Physical Time Step
Exp	experiment		SW	Solid Wall
H	injection throat height		SCT	Self-recirculation Casing Treatment
L_1	axial distance between the trailing edge of the injection and the leading edge of the blade		SMI	Stall Margin Improvement
			W_{bl}	width of the bleeding port
L_2	axial distance between the leading edge of the bleed port and the leading edge of the blade		W_{in}	width of the injection port
			α	jet angle
			β	bleed angle

1. INTRODUCTION

With researchers' further exploration of the internal flow of aero-engines, the compressor design method is becoming increasingly advanced. The single-stage compressor performance has been continuously strengthened and the compressor load has also been increased. The increase in the compressor load will increase the adverse pressure gradient. Moreover, the rotor tip leakage and the degree of the annular wall boundary layer

separation will be further increased as well, thereby leading to a decrease in the stable working range of the compressor (Donald *et al.* 1998). In this case, certain methods need to be taken to improve the compressor stability. In the research upon the casing treatment technology, Prince *et al.* (Prince *et al.* 1974; Rabe and Hah 2002; Wilke and Kau 2002; Nezym 2004) did a lot of research on the casing treatment. They found that the groove and slot casing treatment can effectively improve the stall margin of the compressor, while almost reducing the compressor efficiency. However, self-circulation casing

treatment (SCT) can improve the compressor stability with fewer impacts on compressor efficiency. In this case, the SCT has gained increasing attention from researchers. Research on SCT began in the last century. Griffin (Griffin and Smith 1966, 1970) first proposed the concept of SCT in the experimental research of a single-stage compressor in the 1960s. Later, in 2000, Kenneth *et al.* (2000) used numerical simulations on a moderate-speed fan rotor, and explored the influence of the SCT with different positions of the injection and bleeding part on the compressor. In conclusion, the main reason why the SCT can improve the compressor stability is that the injecting flow with a high relative velocity energizes the low momentum fluid near the end wall.

The influence of SCT on the transonic rotor is studied by Yang *et al.* (2003). The results show that the SCT can weaken the rotor tip clearance leakage vortex. And the rotor obtained 4.4% stall margin improvement because of the SCT. From 2009 to 2018, Zhang (Zhang *et al.* 2009，2010, 2013, 2015, 2016; Wei *et al.* 2018) conducted a series of studies on a subsonic compressor rotor and a transonic compressor rotor, respectively. The results show that on both the subsonic compressor rotor and the transonic compressor rotor, the self-circulation casing treatment can effectively restrain the leading edge spillage and the development of the clearance leakage vortex in the tip passage. The self-circulating casing treatment can also improve the inlet flow angle near the blade tip, and enhance the flow capacity of the blade tip passage.

In 2011, Weichert *et al.* (2011) conducted an experiment on a compressor, and the results show that the SCT with 24 self-recirculation parts provides a stall margin improvement of 6.1% with a peak efficiency loss of 0.8%. Moreover, the stall margin improvement is reduced to 2.6% with the 12 self-recirculation devices. In order to analyze the mechanism of SCT on the compressor, the unsteady numerical simulation was carried out by Khaleghi (2014) on NASA Rotor 67 in 2014. A casing treatment was designed with 22 self-circulating devices in the circumferential direction. Each device of the self-circulating is provided with a 45-degree circumferential skew angle to reduce the loss caused by the vortex. It is found that the tip leakage vortex and passage shock wave are periodically pushed backward by the self-circulating casing treatment.

Jichao *et al.* (2014) experimentally studied on the SCT with different bleed air methods on a transonic compressor test rig. The experimental results demonstrate that the SCT effectively can make the compressor work at a smaller flow rate, and the SMI of 8%-15% can be obtained. At the same time, the peak efficiency can also be slightly enhanced. Jichao *et al.* (2018) also comprehensively studied the application of self-recirculating injection in two different axial flow compressors, and found that the two compressors can work at a smaller mass flow operating point because the injection effect of SCT. Chengwu *et al.* (2014) conducted a numerical study on the NASA Rotor 37, and found that adopting a new SCT with multiple cylindrical holes can provide

a mass flow stall margin improvement of 6.2% with a peak efficiency loss of 0.23%.

In 2019, Kumar *et al.* (2019) studied the influence of injection skew angle (± 30°, ± 47° and +53°) on a transonic axial compressor stage, and found that at the design speed, the self-circulating casing treatment with an injection skew angle of +47° exercises the best effect of extending the compressor stability. Besides, it can provide stall margin improvement of 9.6%. Experiments were conducted by Kumar *et al.* (2022) over the influence of SCT on the aeroelastic aspects of an axial compressor stage. A conclusion was obtained that the SCT can effectively reduce the blade amplitudes. Additionally, the SCT can also reduce casing vibration amplitudes by about 37–69%. Kumar *et al.* (2021) also experimentally and numerically studied the effect of SCT with the injection skew angle on the compressor stability. The result shows that the SCT with an injection skew angle of 0-degree is the best one to improve the compressor stability. For this configuration, the stall margin improvements vary from 6.3% to 9.35% under different investigated speeds.

To sum up, SCT has been extensively investigated by scholars, and several valuable conclusions and experiences for SCT have been obtained. However, by reviewing studies on the SCT, it can be found that the radial inclined angle of SCT, i.e., the angle between the SCT and the radial direction, is 0°, as shown in Fig. 1. Researches on slot casing treatment (Zhang *et al.* 2018, 2020; Wenhao 2020; Zhang *et al.* 2022) indicate that a reasonable radial inclined angle can further improve the compressor stability and reduce the compressor efficiency loss. To explore whether the radial inclined angle can improve the SCT's capability of increasing the compressor stability, some kinds of SCTs with different radial inclined angles were hereby investigated. The purpose of the study is as follows:

1. To reveal the effect of different radial inclined angles of SCT on the performance and stability of the compressor.

2. To explore the flow mechanisms of affecting the compressor with different radial inclined angles of SCT.
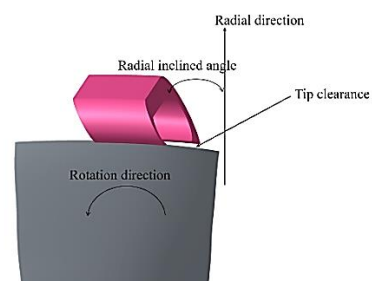

Fig. 1. Schematic diagram of the radial inclined angle of the SCT.

2. INVESTIGATED ROTOR AND SCT

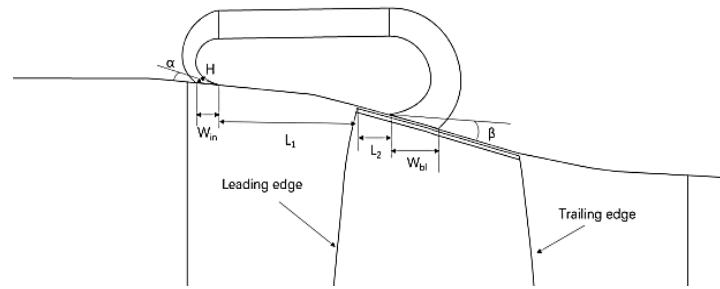The NASA Rotor 35 was chosen for the numerical investigation. Experimental data on the compressor

Fig. 2. Schematic diagram of the structure of the SCT.

Table 1 Key design parameters of NASA Rotor 35

Parameter	Value
Design rotational speed(rpm/min)	17188.8
Design pressure ratio	1.87
Aspect ratio	1.19
Tip clearance(mm)	0.36
Design flow (kg/s)	20.1
Design isentropic efficiency	0.865
Hub radio	0.7
Blade number	36

Table 2 Basic design parameters of the SCT

Parameter	Value
α （°）	10
β （°）	10
L1/Ca	0.86
L2/Ca	0.2
H/Ca	0.06
W_{in}/Ca	0.14
W_{bl}/Ca	0.30

performance can be found in the related reference (Zhang *et al.* 2022), and the design parameters of the rotor are shown in Table 1.

As mentioned above, the radial inclined angle of SCTs is defined as the angle between the SCT and the radial direction, as shown in Fig. 1. In the SCT designing process, the bleed port is placed in the rotor passage, and the injection position is moved to the upstream of the blade passage. On this basis, the present research was carried out by changing the radial inclined angles of SCT, with a Conda curve used for the bleeding and injection parts of the SCT.

Figure 2 depicts the structure diagram of the SCT, where, H represents the throat height of the injection; W_{in}, the width of the injection port; W_{bl}, the width of the bleeding port; L1, the axial distance between the trailing edge of the injection and the leading edge of the blade; L2, the axial distance between the leading edge of the bleed port and the leading edge of the blade; α and β, the jet angle and bleed air angles, respectively; The injection throat height is a constant. The bleeding port was placed above the main blockage areas of blade tip passage with SW, which could effectively reduce the blockage degree of the blade tip passage. Based on previous research experience. The length of bridge part should not be too short. And if the position of the injection port is too far away from the blade, the efficiency loss will be large. Therefore, the injection port shall be placed at a relatively reasonable position. We adopted single passage calculation and one passage had one self-circulation casing treatment device. In the same words, there were 36 passages. And 36 self-circulation casing treatment devices were uniformly distributed in the circumference.

The circumferential coverage rate of the hereby designed SCT is 40%, and the radial inclined angles are 0°, 30°, and 60°, respectively. In the following text, D0, D30, and D60 were used to represent these three SCTs, respectively. Table 2 shows the specific values of the basic design parameters of the SCT. The value of the α should be as small as possible to ensure that the airflow only affects the tip of the blade. Besides, the value of β should also be small, when, the airflow can more smoothly enter the bleeding part. The bleeding port is located near the blockage area when the compressor with SW is stalled, and the injection position is moved to the upstream of the blade passage. The Ca represents the length of the blade tip axial chord.

Figure 3 describes the schematic diagram of the three-dimensional structure of three SCTs with different radial inclined angles, denoted with D0, D30 and D60, respectively. The black arrow represents the blade movement direction. Different radial inclined angles are achieved by rotating the profile of the self-circulating structure in the IGG module of NUMECA, and the bridges of SCT with different inclined angles are ensured at the same radius level. Herein, the SCT was divided into different blocks, i.e., the bleeding part, the bridge part, and the injection part, which are shown by the blue, green, and red areas, respectively.

3. NUMERICAL MODEL AND VERIFICATION FOR THE SOLID WALL

3.1 Governing Equations

NUMECA(8.9) software was hereby used to solve the RANS equations in the relative coordinate system. Eq．(1) details the RANS equations in the integral form of the control volume *Ω*.

$$\frac{\partial}{\partial t}\int_{\Omega} U d\Omega + \int_{S}\vec{F}_{I}\cdot d\vec{S} + \int_{S}\vec{F}_{V}\cdot d\vec{S} = \int_{\Omega} Q_{T} d\Omega \quad (1)$$
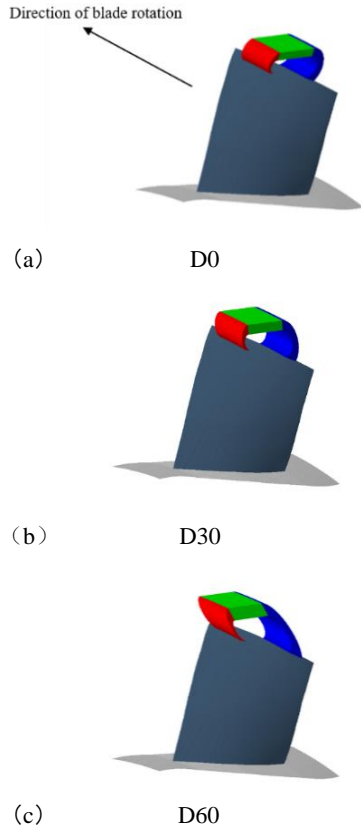

(a)   D0

（b）   D30

(c)   D60

Fig. 3. Schematic diagram of the 3D structure.

$$U = \begin{bmatrix} \bar{\rho} \\ \bar{\rho}v_1 \\ \bar{\rho}v_2 \\ \bar{\rho}v_3 \\ \bar{\rho}\tilde{E} \end{bmatrix} \vec{F}_I = \begin{bmatrix} \overline{\rho v_i} \\ \overline{\rho\tilde{v}_1 v_i} + \overline{p^*}\delta_{1i} \\ \overline{\rho\tilde{v}_2 v_i} + \overline{p^*}\delta_{2i} \\ \overline{\rho\tilde{v}_2 v_i} + \overline{p^*}\delta_{3i} \\ (\overline{\rho E} + \overline{p^*})v_i \end{bmatrix} \vec{F}_V = \begin{bmatrix} 0 \\ \bar{\tau}_{i1} \\ \bar{\tau}_{i2} \\ \bar{\tau}_{i3} \\ \bar{q}_i + \tilde{v}_i \bar{\tau}_{ij} \end{bmatrix} \quad (2)$$

$$Q_T = \begin{bmatrix} 0 \\ -\bar{\rho}\left[2\vec{\omega}\times\vec{w} + \left(\vec{\omega}\times\left(\vec{\omega}\times\vec{r}\right)\right)\right] \\ \overline{\rho\vec{w}}\cdot\vec{\nabla}\left(0.5\omega^2 r^2\right) \end{bmatrix} \quad (3)$$

Where, U, $\vec{F}_I$ and $\vec{F}_V$ represent independent variables, vector (column matrix) of inviscid flux, and vector (column matrix) of viscous flux, respectively; Q_t, source term; $\overline{A}$, the time averaged value; $\tilde{A}$, the corresponding density weighted average value; A_1, A_2, and A_3, the components along three coordinate directions in the three-dimensional coordinate system; and τ, the stress tensor.

The Reynolds stress components is given by:

$$\bar{\tau}_{ij} = (\mu_t + \mu)\left[\frac{\partial\bar{v}_i}{\partial x_j} + \frac{\partial\bar{v}_j}{\partial x_i} - \frac{2}{3}\left(\vec{\nabla}\cdot\vec{v}\right)\delta i_j\right] \quad (4)$$

Where, μ_t denotes the coefficient of dynamic viscosity; and κ, the coefficient of dynamic viscosity. μ_t and κ_t should be calculated by the turbulence models. The static pressure and the total energy are defined as:

$$\overline{p^*} = \bar{p} + \frac{2}{3}\bar{\rho}k \quad (5)$$

$$E = \tilde{e} + \frac{1}{2}\tilde{v}_i\tilde{v}_i + k \quad (6)$$

The more details can see in the NUMECA manual.

3.2 Numerical Model

Figure 4 shows the computational domain mesh, the mesh of the blade-to-blade surface and the computing domain grid of the SCT. Single passage calculation was hereby adopted, and the entire passage grid was divided into three regions along the airflow direction, i.e., the upstream part, the rotating part, and the downstream part. Table 3 shows the grid distribution in this paper. The O topology and butterfly topology were used to the blade passage and the blade tip clearance. The total grid number for one compressor passage with SCT is more than 1.33 million.

Table 3 Grid distribution.

	O topology grid	Butterfly topology grid
Radial	101	17
Tangential	21	17
Axial	161	161
Total grid number	1080000	

Based on our previous research experience (Zhang *et al.* 2022) the numerical calculation has already satisfied the grid-independent requirements, in the case of over 700,000 single-passage grids. The number of the hereby used single-passage grids exceeds 1 million, so the grid independence verification was no longer carried out.

The numerical simulation adopted the 3D unsteady calculation. The second-order upwind method was adopted for spatial discretization scheme, and the time discretization of the governing equations was completed using the four-order Runge-Kutta method. In unsteady calculation, the physical time step(PTS) of one blade passage was set to 20, while the inner iterations were 20 steps. Based on our previous research experience (Zhang *et al.* 2022), the Spalart-Allmaras (SA) model was selected as the turbulence model for this numerical simulation. In the steady calculation, the completely unmatched frozen rotor method was used between rotating-stationary
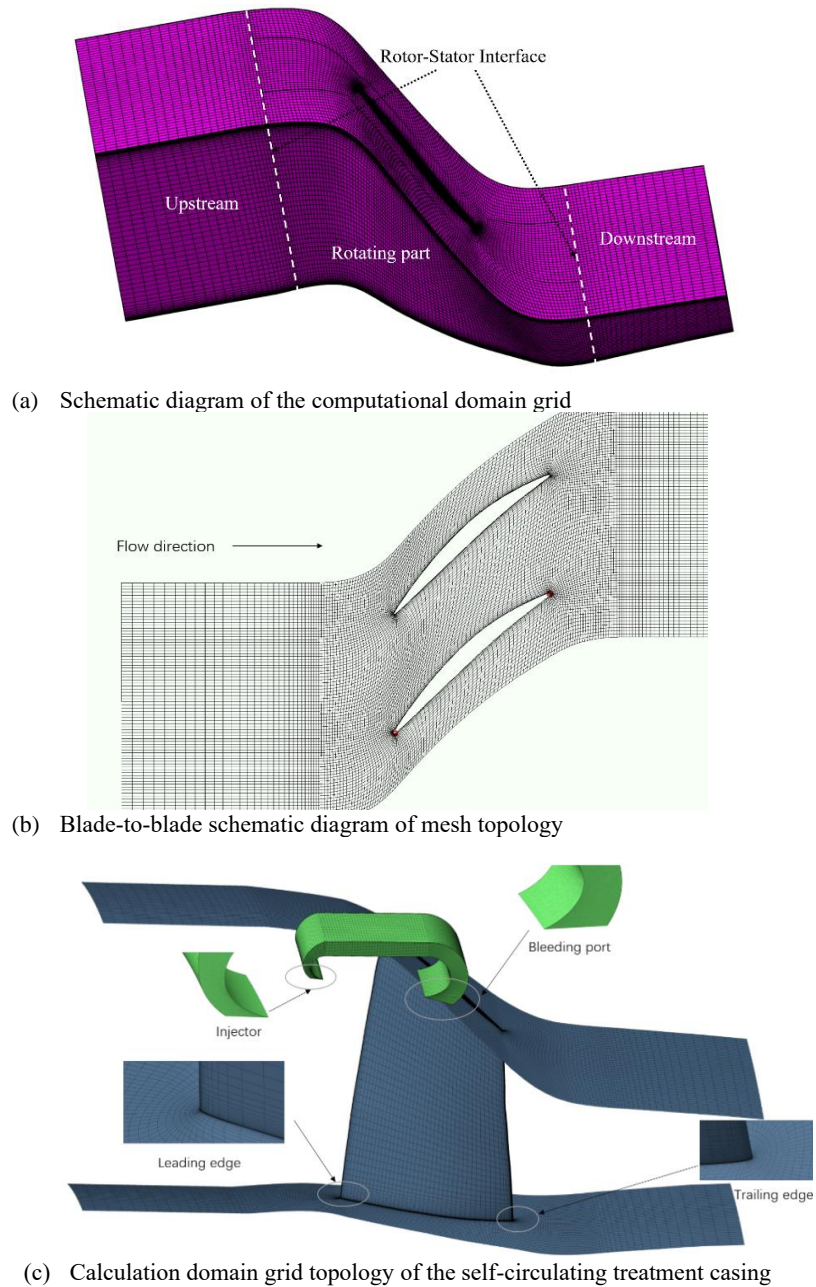
(a) Schematic diagram of the computational domain grid

(b) Blade-to-blade schematic diagram of mesh topology

(c) Calculation domain grid topology of the self-circulating treatment casing

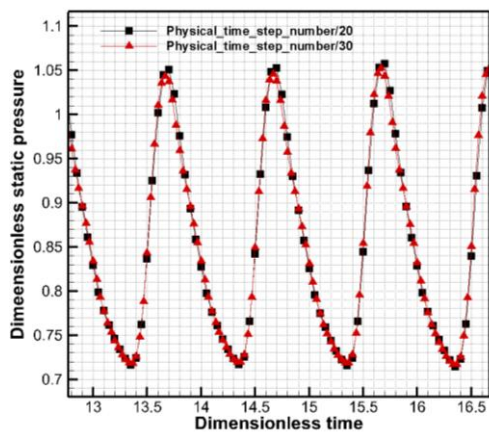**Fig. 4. Schematic diagram of mesh division.**

Fig. 5. Dimensionless static pressure distribution on a SCT wall for D0 at the near stall point.

interfaces to complete the data transfer, and the unsteady calculation was changed to the area scaling method.

We compared difference between 20PTS and 30PTS at the near stall point for D0 to verify the independence of the physical time step. Figure 5 shows the dimensionless static pressure distribution on a SCT wall between 20PTS and 30PTS. The static pressure is dimensionless by a standard atmospheric pressure (101325Pa). It is noteworthy that the dimensionless time for 1 means one blade rotates one blade passage. As can be seen in Fig. 5, the static pressure calculated with 20PTS is basically consistent with that calculated with 30PTS on the same SCT wall. Besides, Table 4 depicts that the results of 20PTS are almost consistent with those of

Table 4 Comparison between two kinds of physical time steps

Type	Total pressure ratio	Adiabatic efficiency
PTS=20	2.0202	0.7461
PTS=30	2.0216	0.7468

30PTS. Therefore, it is acceptable for us to choose 20PTS for the numerical simulation.

In the calculation settings of numerical simulation, the inlet total pressure and the inlet total temperature were 101325 Pa and 288.15 K, respectively. The average static pressure was hereby selected for outlet conditions. In the process of numerical simulation, the performance parameters of different mass flow rates were obtained by continuously increasing the average static pressure value of the compressor outlet. When the compressor approached the near-stall point, the difference in the back pressure between the last stable operating point and the stall point was 100Pa.

3.3 Verification for SW

Figure 6 shows the compressor performance curve by the experiment and numerical simulations. The experimental results are given in the reference (Lonnie and Moore 1978). The unsteady calculation performance curve is time-averaged solution by the results of 20 physical time steps. It can be observed from Fig. 6(a) that the unsteady calculated total pressure ratio curve is above the steady curve as a whole, especially under small and medium mass flow conditions. The results of the unsteady calculations at each mass flow rate are more consistent with the experiment values. Figure 6(b) reveals that the unsteady calculated peak efficiency is also higher than the steady prediction value. On the whole, the total performance curve obtained by the unsteady calculation is rather close to the experimental result.

Figure 7(a) depicts the distribution of the total pressure ratio along the blade span at the near-stall condition, and Fig. 7(b) shows the distribution of the isentropic efficiency along the blade span at the design point. The experimental results are given in the reference (Lonnie and Moore 1978). As far as the total pressure ratio near the stall is concerned, the calculated total pressure ratio at each steady state is smaller than the actual value in most positions. However, the unsteady calculated value is highly consistent with the measured value along the blade span. For the prediction of the compressor design point efficiency, the results of unsteady calculations
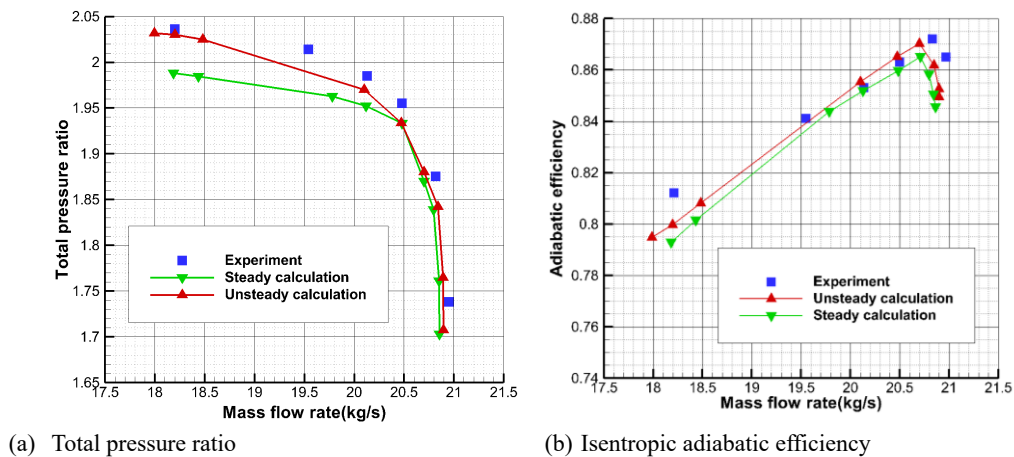

(a) Total pressure ratio   (b) Isentropic adiabatic efficiency

Fig. 6. Compressor total performance curves.

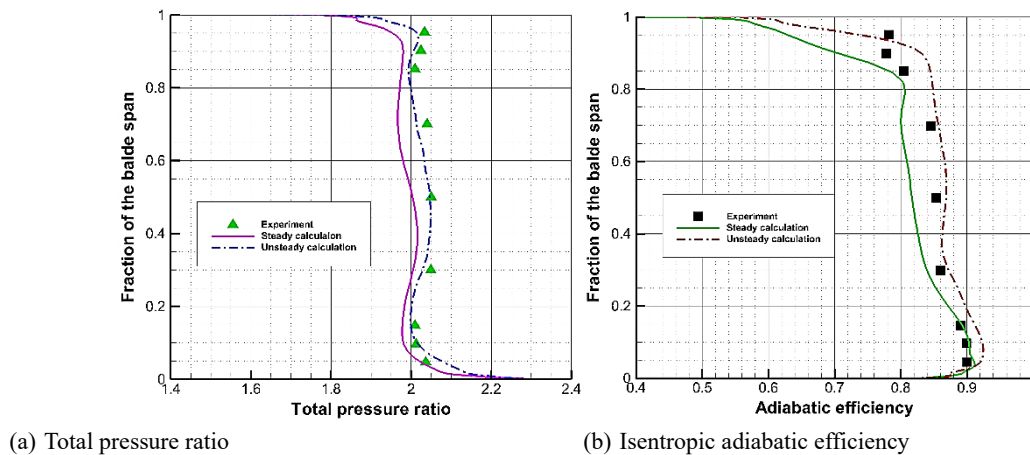(a) Total pressure ratio   (b) Isentropic adiabatic efficiency

Fig. 7. Comparisons of rotor outlet flow parameters.

are generally closer to the actual values. Taken together, unsteady calculations can accurately predict the compressor performance.

4. RESULTS

4.1 Compressor Performance Analysis

Figure 8 shows the performance curves of solid wall (SW) and self-circulation treatment (SCT) withdifferent radial inclined angles. The mass flow rate of the operating points was hereby normalized by the maximum mass flow rate of SW.

On the whole, the stall mass flow rate of compressor becomes smaller regardless of the adopted SCT. The self-circulating structure with a radial inclined angle can further broaden the stable working range of the compressor compared with the one without the radial inclined angle. The near-stall mass flow rates of D30 and D60 are rather close, but compared with the D30, D60 can work steadily at a smaller mass flow rate.

In terms of the total pressure ratio, D30 and D60 have a little increase than D0 after the normalized mass

flow rate of 0.9617, i.e., the compressor design point. The increase is more obvious after the 0.85 mass flow rate. It shows that the SCT with a radial inclined angle can further improve the pressurization capability of the compressor under small mass flow rate conditions. Before the mass flow rate of the design point, the curves of the three SCTs are basically coincident. The choke mass flow rate of the SCTs is smaller than that of the SW.

In terms of the isentropic adiabatic efficiency, there are no significant differences in the peak efficiency of the SCTs with three inclined angles, and the efficiencies of SCTs are all lower than the peak efficiency of the SW. In the range after the peak efficiency point, the isentropic adiabatic efficiencies of the three SCTs are higher than those of the SW.

In contrast, the efficiency of D30 is always greater than that of the other three, but the differences among all four casings are rather limited. Within the range from the design mass flow rate to the near-stall mass flow rate, the curve of D60 is above that of D0. It can be seen that the increase of the radial inclined angle can to some extent reduce the loss, thereby slightly improving the compressor efficiency.
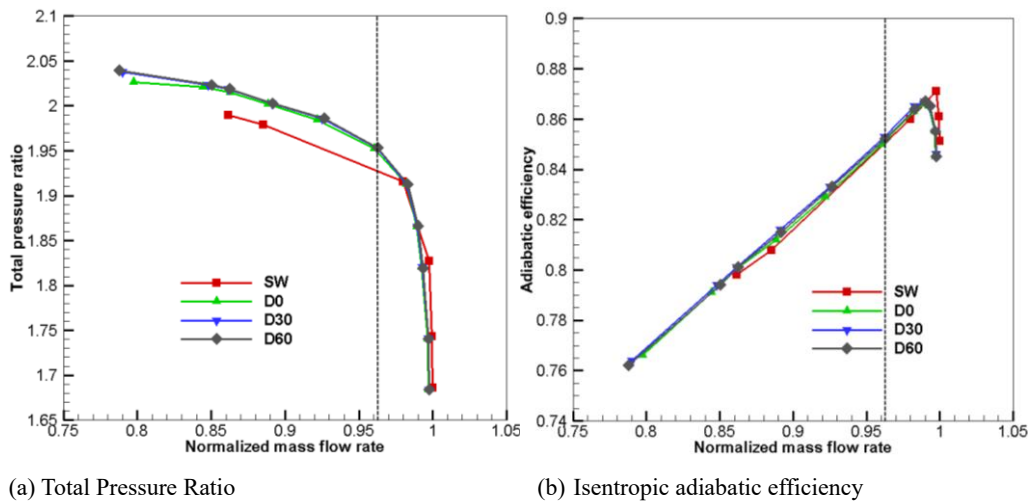

(a) Total Pressure Ratio

(b) Isentropic adiabatic efficiency

Fig. 8. Performance curve of SW and SCT.

Table 5 Comparison between SW and SCT.

	η_P^*	η_S^*	π_S^*	m_S	SMI	PEI	DEI
SW	0.8708	0.8482	1.991	0.8617			
D0	0.8655	0.8512	2.026	0.7976	9.94%	-0.61%	0.35%
D30	0.8651	0.8522	2.038	0.79	11.66%	-0.66%	0.47%
D60	0.8649	0.8531	2.039	0.7876	12.05%	-0.68%	0.58%

Table 5 intuitively shows the stall margin improvement (SMI), the peak efficiency improvement (PEI), and the design point efficiency improvement (DEI) of the SCTs with three different radial inclined angles.

The stall margin increase is defined as:

$$SMI = \left[\left(\frac{\pi_{CT}^*}{m_{CT}} \right)_{stall} - \left(\frac{\pi_{SW}^*}{m_{SW}} \right)_{stall} \right] / \left(\frac{\pi_{SW}^*}{m_{SW}} \right)_{stall} \times 100\% \quad (7)$$

The peak efficiency improvement is defined as:

$$PEI = \left[\frac{(\eta_{Peak}^*)_{CT}}{(\eta_{Peak}^*)_{SW}} - 1 \right] \times 100\% \quad (8)$$

The design point efficiency improvement is defined as:

$$DEI = \left[\frac{(\eta_{Design}^*)_{CT}}{(\eta_{Design}^*)_{SW}} - 1 \right] \times 100\% \quad (9)$$

In Formula (7), π^* and m represent absolute total

pressure ratio and mass flow respectively. In Formulas (8) and (9), the rotor efficiency is denoted by η^*. CT is the short name for the casing treatment.

It can be observed from Table 5 that the increase of the radial inclined angle further enhances the SCT's ability to increase the compressor stability. The SMI of D60 has reached 12.05%. Compared with D0, the SMI of D60 is further increased by 2.11%, while that of D30 is 11.66%. As far as the peak efficiency is concerned, D0, D30 and D60 are almost the same. The relative changes of peak efficiency are less than 0.1%. With the increase of the radial inclined angle, only slight increase can be observed in the compressor efficiency for the design point.

4.2 Flow Field Analysis for SW and SCT

Related references have shown that the stall of Rotor 35 is caused by tip blockage (Zhang *et al.* 2022). Figure 9 shows the relative Mach number distribution of the SW and the compressor with different radial inclined angles SCT at the blade span of 98% at the same instantaneous time. The normalized mass flow rate of different SCTs remains the same, and the SW is under a near stall condition (The normalized flow rate is 0.8617). Subsequent analyses are mostly based on the same working conditions, so this description will not be repeated next. The position of the shock wave is given by the red line in the figure. By comparing Fig. 9 (a) with Fig. 9 (b), it can be observed that the range of the low relative Mach number region in the passage has been reduced in D0. After the application of D0, the circumferential size of the low relative Mach number

region has also been reduced. The flow capacity on the pressure surface side of the blade in the passage has been enhanced due to the elimination of the low-velocity region. The size of the low-velocity region in the axial direction is reduced by about 2/3. The position and shape of the shock wave are also significantly changed under the influence of the SCT. The inflection point of the shock wave near the suction side of the blade moves forward greatly. The shape of the shock wave at the entrance of the passage is smoother and is basically perpendicular to the middle of the suction side. The Mach number does not decrease suddenly or sharply after the airflow passed the shock wave. The distribution of relative Mach number in the passage is more uniform.

With the increase of the radial inclined angle, the ability of SCT to eliminate the low-velocity region at the tip passage entrance is found to be enhanced. In the first half of the tip passage, the low Mach number region of D30 decreases significantly, only about 1/4 of that of D0. The effect of D60 on improving the flow capacity is strongest. The region where the Mach number is lower than 0.25 at the entrance of the passage is eliminated. In contrast, the SCT with a radial inclined angle of 60°can ensure the flow capacity of the blade tip passage inlet to the greatest extent and effectively stabilize the compressor flow condition.

After adopting different SCTs, the boundary layer separation of the compressor in the blade tip trailing edge changes basically. The starting position of the boundary layer separation area with different radial inclined angles is almost the same, and the smaller circumferential size of the boundary layer separation
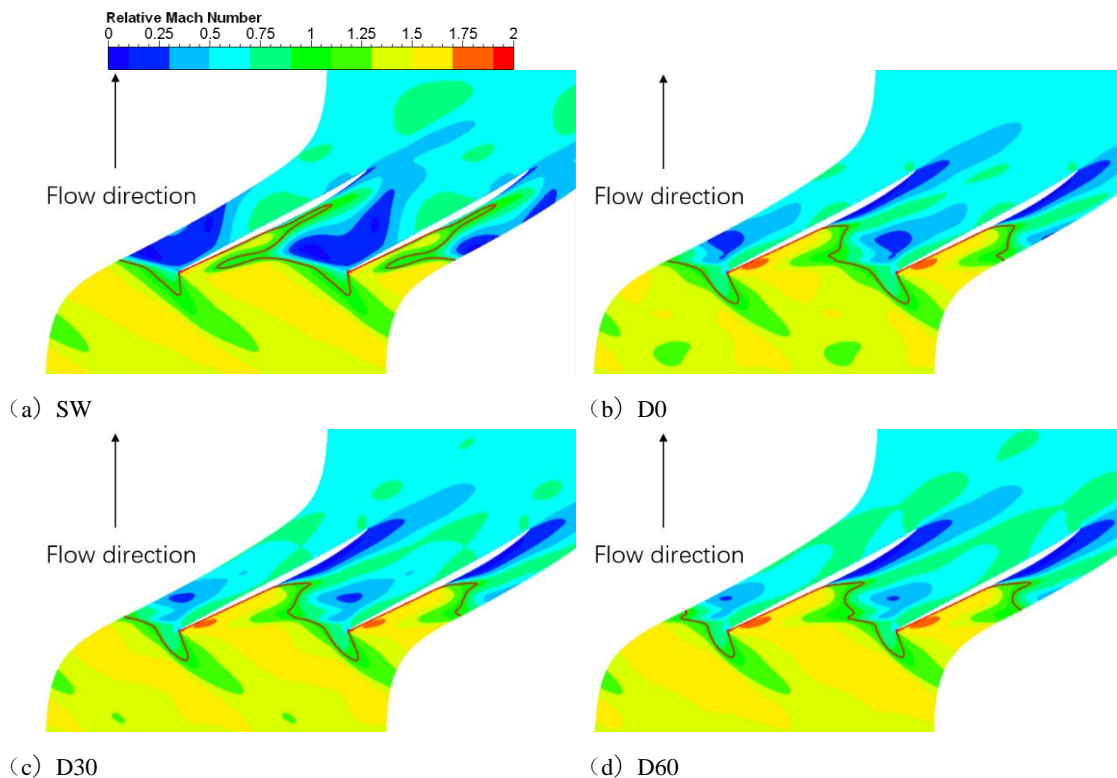

(a) SW   (b) D0   (c) D30   (d) D60

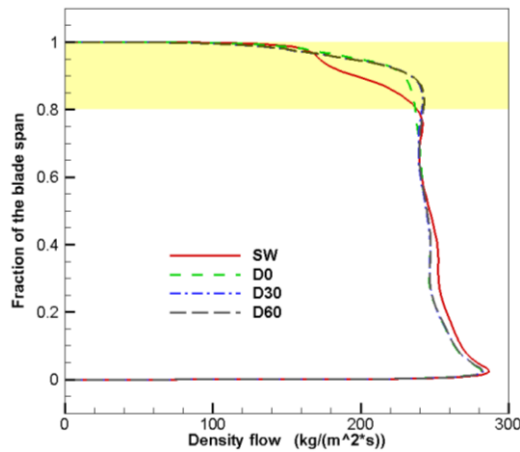**Fig. 9. Relative Mach number at the 98% blade span.**

Fig. 10. Density flow along the blade span.

area fails to exercise a significant impact on the flow in the passage.

The circumferential average distribution of the time-averaged density flow along the blade span is vividly depicted in Fig. 10, with the density flow defined as the flow axial velocity (V_z) multiplied by the local density (ρ). It can be seen that the density flow of the three SCTs below 70% blade height is basically the same.

Due to the blockage effect in the tip passage, the upstream airflow fails to pass through SW completely. In this case, the density flow at the outlet decreases significantly near the blade tip. In the range of 80% to 97.5% blade span, the density flow of the SCTs is greater than that of the SW, indicating that in this blade span range the SCT improves the flow capacity in the passage. In the range of 70% to 95% blade span, the density flow of D0 is slightly smaller than that of D30 and D60, suggesting the better performance of the SCT with radial inclination angle in improving the passage's flow capacity in the blade span range. However, above 95% blade span, the density flow of D0 is slightly higher than that of D30 and D60. Above 97.5% blade span, the density flow of SW is greater than that of three kinds of SCTs. In the whole range of blade span, the density flow curve of D30 almost coincides with that of D60. However, overall, within the range of 80% to 97.5% blade span, the SCTs can better improve the flow capacity in the passage. Compared with D0, D30 and D60 have a larger range and a higher degree of improvement on the flow capacity.

Figure 11 exhibits the streamline distribution for the tip leakage flow of the SW and SCT at the same time. The leakage streamline of D0 at the leading edge is more concentrated than that of SW. For the occurrence of leading-edge spillage and secondary leakage, the SCT matters considerably in restraining it. The leading-edge spillage in the passage is basically eliminated, but there is still a phenomenon that the leakage streamline is crossing the blade tip into the next passage in the last half of the blade tip. Compared with D0, the SCTs with the radial inclined angle further strengthen the concentration of the leakage streamline at the position of the flow bleeding part. Besides, the leading-edge spillage
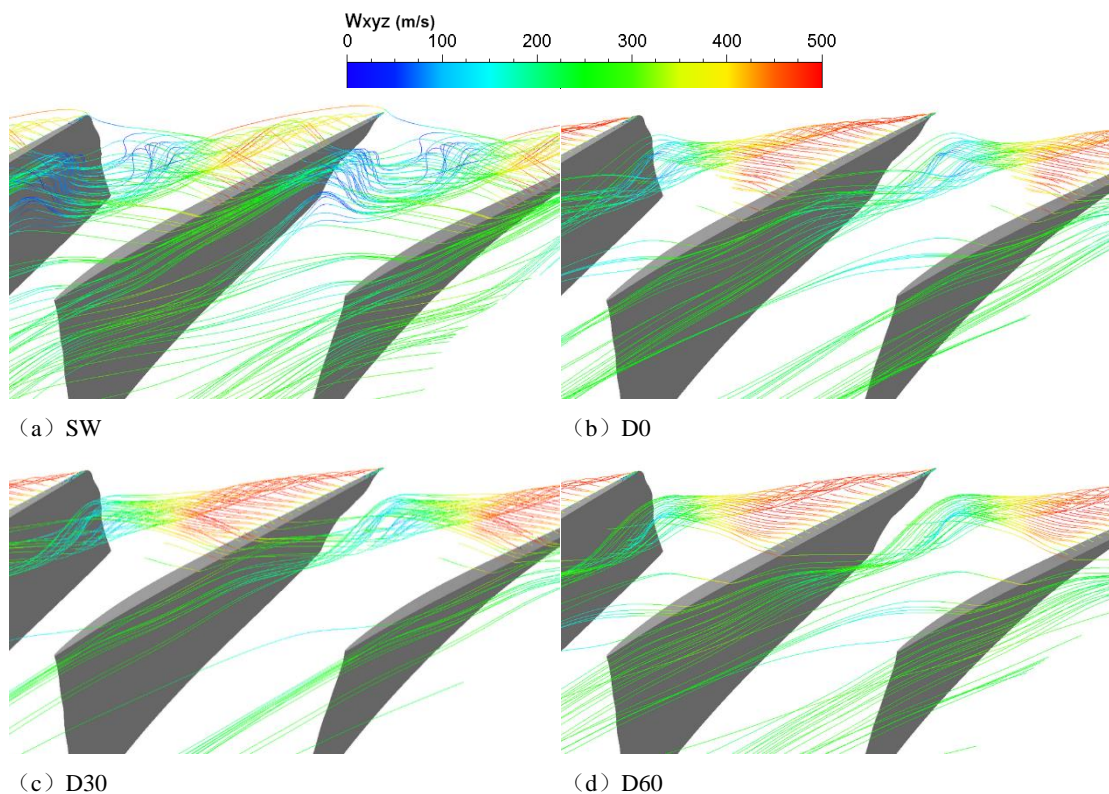

（a）SW

（b）D0

（c）D30

（d）D60

Fig. 11. Distribution of the tip clearance leakage flow.

phenomenon disappears, while the secondary leakage phenomenon still exists. Also, this phenomenon is hardly different under the action of different SCTs. However, compared to the SW, it also has a significant reduction. On the whole, the SCTs with different radial inclined angles can control the distribution form of the leakage streamline, and can reduce the passage blockage caused by the expansion and diffusion of the leakage flow.

Figure 12 shows the axial blockage ratio at different times for SW and SCTs. The blockage ratio is defined as the ratio of the region where the axial relative velocity (WZ) is less than zero to the entire region.

Besides, 20 physical time steps can be considered a complete compute cycle. On the whole, it can be seen that the distribution of the blockage ratio shows an obvious periodicity. At the initial moment (T0) of a complete cycle, the SW has a large blockage in the axial range of 10%Ca to 35%Ca. As time goes on, the large blockage ratio area gradually moves backward and remains below 50%Ca. The large blockage ratio area basically disappears at T12 in the cycle, and it will keep this condition until T15. After T15, the passage blockage ratio increases

significantly in the axial range of 20%-30%Ca. In the remaining time, the axial range of the large blockage ratio area further expands until it becomes the same as the initial time, and then enters the next same cycle. In contrast, the blockage ratio of D0 over the whole cycle is lower than that of SW, and the axial dimensions with large blockage ratios are always kept within a small range. From T4 to T10, there is basically no large blocking ratio area in the passage. The whole blade passage has a good flow capacity at all times. The time of D0 which keeps a small blockage ratio area is longer than that of SW.

Compared with D0, the development of the large blockage ratio area in the period is basically the same.

From T12 to T18, the passage blockage ratio increases significantly in the axial range of 20%-30%Ca, while the maximum blockage ratio of D30 is lower than that of D0. The blockage ratio in the first half of the passage of D30 is generally lower than that of D0. When the radial inclined angle increases to 60°, the change of blockage ratio is more obvious. There is no area with a blockage ratio greater than 0.25 in the passage. From T8 to T12, the blockage ratio of the passage increases in the axial
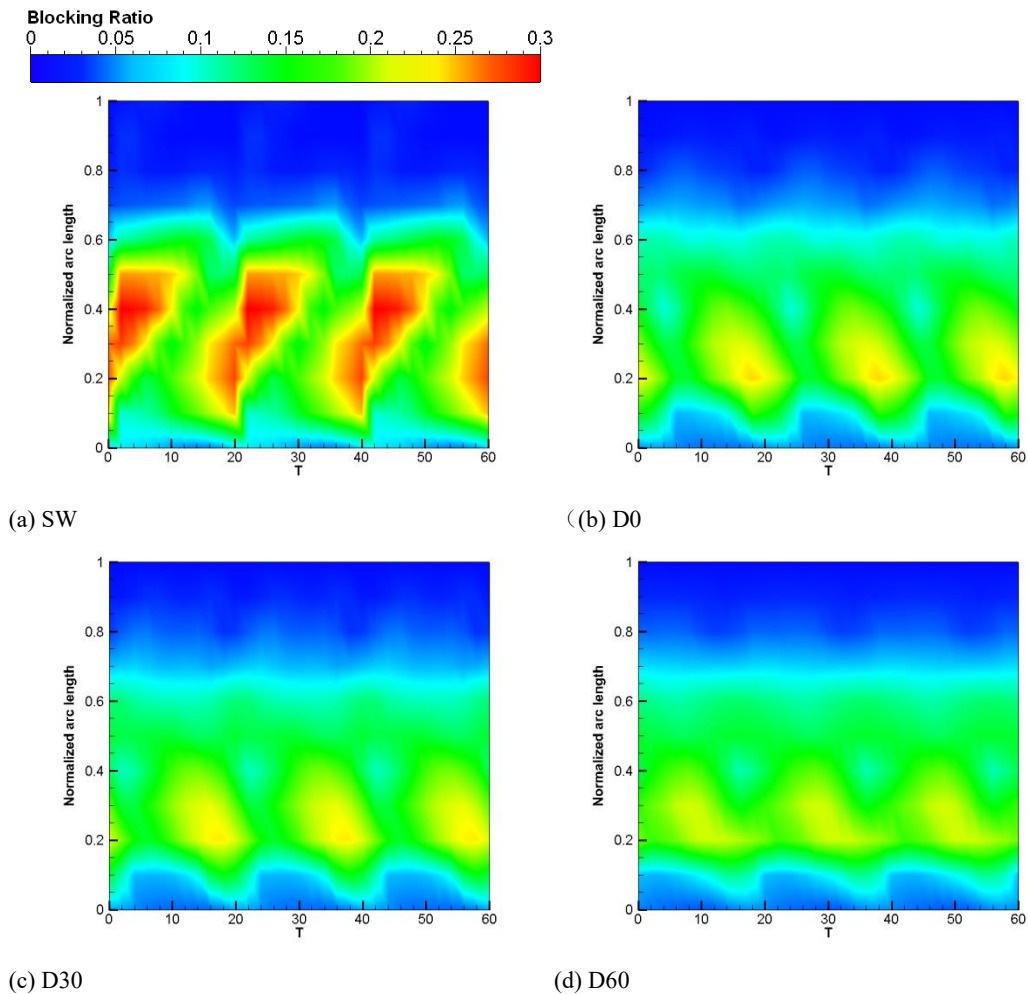
.

(a) SW   （b) D0

(c) D30   (d) D60

Fig. 12. Axial distribution of blockage ratio at different time.
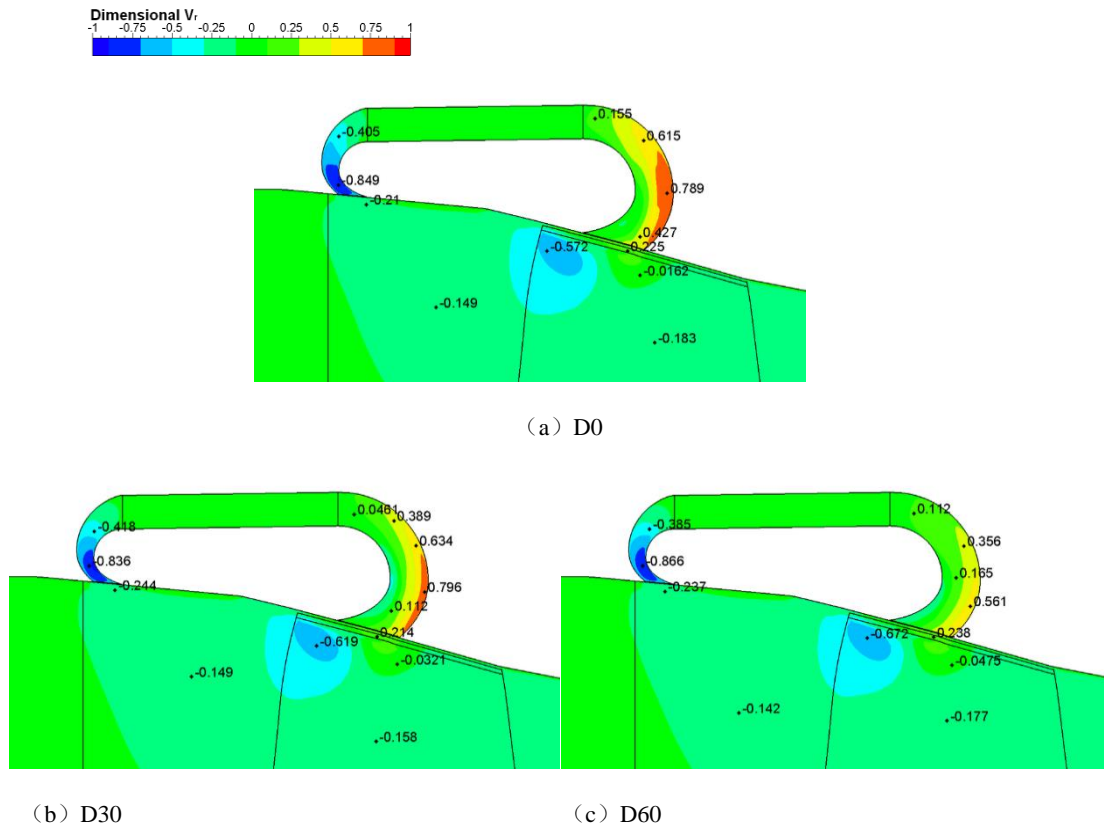
（a）D0

（b）D30

（c）D60

Fig.13. Normalized radial velocity distribution on the meridian plane.

range of 20%Ca to 30%Ca. The duration of D60 at a high blockage ratio is shorter than that of D30 at a high blockage ratio. The leading edge of the high blockage ratio area always remains at 20%Ca. For more than half of a cycle, there is almost no high blockage ratio area in the passage. Given that the SCTs with different radial inclined angles maintain the same circumferential coverage, the relative influence time of the three SCTs is consistent. However, D60 has the strongest ability to reduce the passage blockage ratio, indicating that the radial inclined of 60° can further improve the performance of the SCT and more effectively eliminate the blocked area in the passage.

Figure 13 shows the distribution of the normalized radial velocity of the compressor with different SCTs on the meridian plane. The black numbers in Fig. 13 represent the local normalized radial velocity values. In contrast, the SCTs with different radial inclined angles do not make a great change in the radial velocity distribution in the injection part. The radial velocity of the airflow reaches the peak near the injection part. With the increase of the radial inclined angle, the radial velocity of the airflow in the bleeding part decreases significantly. The high radial velocity of D30 near the outer wall surface of the bleeding part decreases significantly compared to that of D0. When the radial inclined angle increases to 60°, the normalized radial velocity of the airflow in the bleeding part is generally less than 0.75.

The flow direction length in the bleeding part is increased when the radial inclined angle is larger

than 0 degree, but the rotation angle of the airflow direction remains unchanged. A larger radial inclined angle of SCT indicates a smoother contour profile of the bleeding part. Hence, the airflow can flow forward more uniformly. This can explain the gradual decrease of the high radial velocity region in the bleeding part with the increase of the radial inclined angle.

Figure 14 shows the absolute Mach number and streamline distribution inside the SCT with three different radial inclined angles. Taking the time average result for analysis, different SCTs take the circumferential section at the same radial height. Considering the large radial inclined angle, the visual angle of D60 is slightly different from that of the other two. Besides, a large region of low Mach number can be observed in the left position of D0, and the low Mach number region is mostly in the bleeding part. The airflow is mixed in the bleeding part to form a large-scale vortex, which is related to the high tangential velocity of the flow when it enters the bleeding part. By deflecting the SCT with a certain angle in the radial direction toward the rotation direction of the blades, the airflow can be buffered in the circumferential motion.

There is a collision effect between the flow and the bleeding par, and the SCTs with the radial inclined angles can alleviate the influence of the collision effect.

Figure 14(b) and Fig. 14(c) indicate that the vortex has disappeared. After entering D30 and D60, the airflow can uniformly flow to the outlet of the
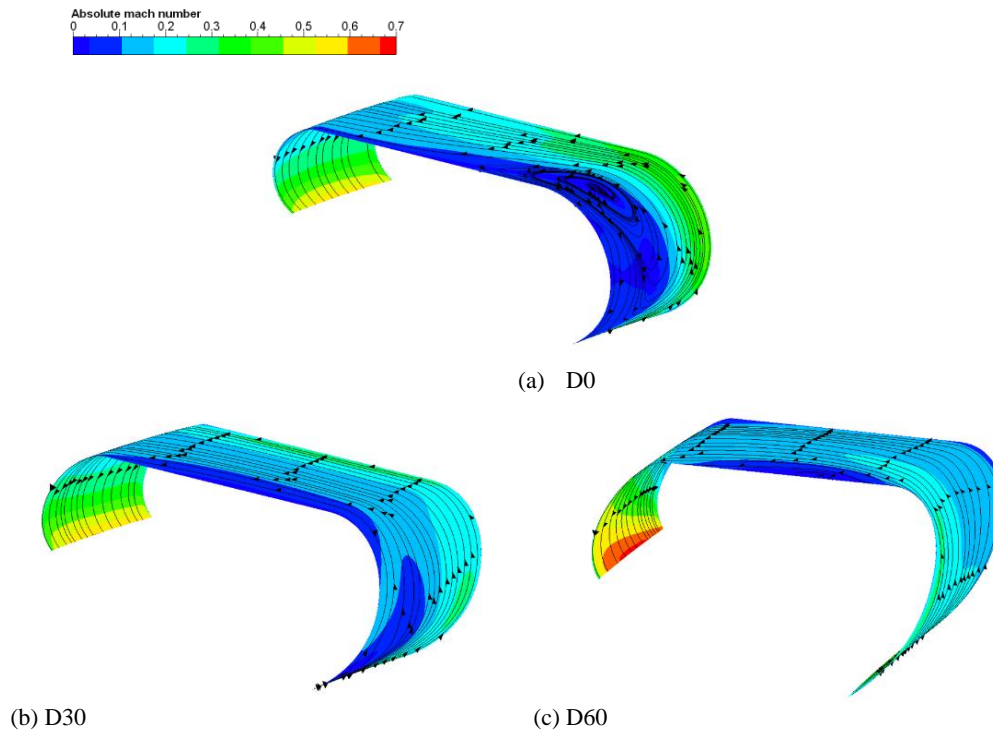
(a) D0

(b) D30   (c) D60

Fig.14 Absolute Mach number and streamline distribution

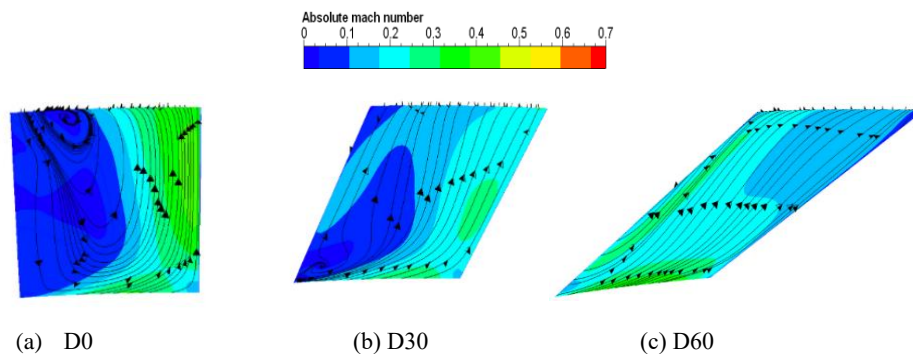(a)   D0   (b) D30   (c) D60

Fig. 15. Absolute Mach number and streamline distribution in the bleeding part.

injection along the flow direction. The absolute Mach number distribution in the bridge passage and the bleeding part of D30 and D60 is more uniform than the distribution of D0. The low Mach number region has been reduced in the SCTs with different radial inclined angles.

In order to more intuitively explain the improvement effect of radial inclined angles on the airflow in the bleeding part, the front view of the absolute Mach number and streamlines distribution in the bleeding part of the three SCTs is clearly demonstrated in Fig. 15. The difference in the shape of the circumferential section leads to the difference in the visual angles of the three figures. Fig. 15 shows that the motion of the airflow in the no radial inclined SCT (D0) entering the bleeding part is a circumferential movement to a sidewall at the beginning. The streamline moving forward is concentrated on the right half, while the left half of the flow passage is filled with swirling airflow. The absolute Mach number of the airflow

has an obvious stratification on the left and right halves.

When the SCT is radially deflected by 30°, the airflow can move smoothly in most of the circumferential inlet range, smoothly enter the bridge, and move forward. The vortex area is basically eliminated in the bleeding part. Only a weak swirl can be observed in the left corner. The airflow on the left side turns upward in the bleeding part quickly, thus resulting in a lower absolute Mach number level on the left side, but a significant improvement relative to D0.

As the radial inclined angle increases to 60°, the wall surface of the SCT at the inlet of the bleeding part is closer to the circumferential direction. The airflow at the inlet can be easily turned to the direction of the flow passage. The larger inclined angle also makes the flow passage of the bleeding air move to the top right. The circulating flow has sufficient time and circumferential range to complete the mixing during
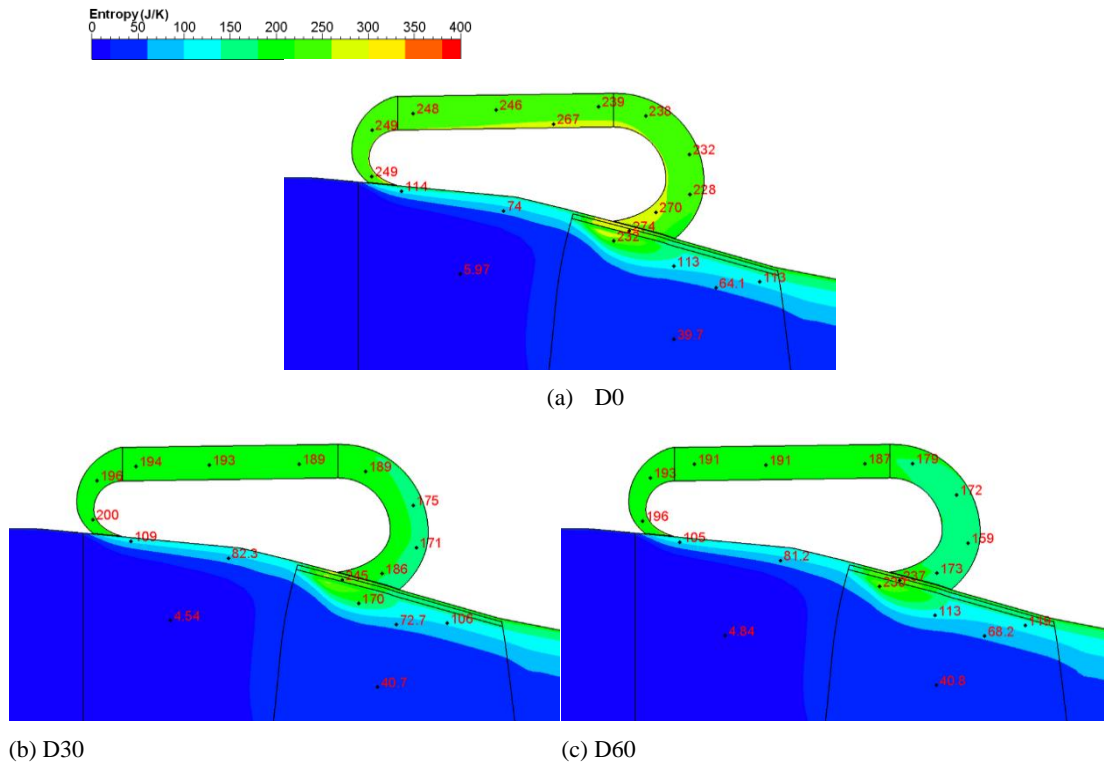
(a) D0

(b) D30

(c) D60

Fig. 16. Entropy distribution on the meridian plane.

the adjustment process. The absolute Mach number distribution of the entire bleeding part is rather uniform, and basically, the area with a low absolute Mach number no longer exists.

Based on the above analysis, it can be claimed that increasing the radial inclined angle can significantly improve the flow condition in the bleeding part, and that D60 has the best effect in comparison. The improvement of the flow conditions in the bleeding part effectively enhances the flow absolute Mach number and increases the flow jet speed. This also explains the greater absolute Mach number of the D60 airflow at the injection part in Fig. 14 than the absolute Mach numbers of D0 and D30.

The effect on the efficiency can be judged by the change of the entropy values. Figure 16 shows the entropy distributed on the meridian plane of SCT with different radial inclined angles. The time-average calculation result of the normalized mass flow rate of 0.8617 was hereby taken as the circumferential average by the three radial inclined angles. The red numbers give the local entropy value. The entropy values of D30 and D60 in the SCT are found significantly lower than that of D0 as a whole. The range of entropy above

250J/K exists in Fig. 16 (a), but basically disappears in Fig. 16 (b) and 16 (c). As the radial inclined angle increases, the entropy value of the bleeding part decreases. Due to the large circumferential velocity of the bleed air in the inlet section, the distribution will be uneven, thereby resulting in strong mixing, and thus inevitably increasing the entropy value. By increasing the radial inclined angle, the airflow mixing can be significantly reduced, the swirling

flow can be eliminated, and the entropy value of the bleeding part decreases as a whole with the increase of the radial inclined angle. Compared with that of D0, the entropy values of D30 and D60 in the injection also show a significant decrease. For the distribution of entropy values within the passage, no obvious change is observed in Fig. 16(a), 16(b) and 16(c).

5. CONCLUSIONS

Investigations were hereby conducted to explore the effect of SCTs with different radial inclined angles on the ability to improve compressor stability. By comparing the unsteady calculated results, it is confirmed that the radial inclined angle does play a role in enhancing the self-circulation casing treatment effect. At the same time, combined with the analysis of the compressor passage and the internal flow of the self-circulating structure, the internal reasons why the SCT with radial inclined angle can improve the compressor stability were clarified. The research conclusions are as follows.

(1) The increase of the SCT radial inclined angle can further improve the stable working range of the Rotor 35. The stability margin improvement is led up to 9.94%, 11.66% and 12.05% by D0, D30 and D60, respectively. The peak efficiency of D30 remains at the same level as that of D60, while the peak efficiency of D30 is about 0.6% lower than that of SW. The compressor design point performance is further slightly improved with the increase of the inclined angle.

(2) With the increase of the radial inclined angle, the self-circulation structure has a stronger

elimination effect on the low Mach number region in the blade tip passage, and the axial distribution range of the high blocking ratio region in the rotor passage is also getting smaller. The entire passage blockage can decrease most of the time in a computing cycle. The flow capacity of the tip passage increases significantly with the increase of the radial inclined angle.

(3) The self-circulating structure is inclined radially toward the rotation direction, and thus optimizes the flow conditions inside the bleeding part. Besides, the airflow distribution in the bleeding part is getting smoother. After the airflow enters the bleeding part, the direction of airflow can be evenly adjusted in the circumferential direction, which avoids the generation of a swirling airflow structure on the left side of the self-circulating passage, and effectively reduces the flow loss caused by the rotating mixing of the airflow in the self-circulating structure. The radial skew gives a certain circumferential velocity to the airflow at the injection, thereby weakening the mixing effect of the jet and the upstream airflow. Overall, the compressor efficiencies of D30 and D60 are slightly higher than that of D0 in the range after the design point mass flow.

FUNDING

REFERENCES

Chengwu Y., S. Zhao, X. Lu, G. Han and J. Zhu (2014). Investigation on multiple cylindrical holes casing treatment for transonic axial compressor stability enhancement. *Journal of Thermal Science* 23(4), 346-353.

Donald, C., S. Tan, H. D. Vo and E. M. Greitzer (1998). Role of blade passage flow structures in axial compressor rotating stall inception. In *ASME 1998 International Gas Turbine and Aero-Engine Congress and Exhibition,* Stockholm, Sweden, GT1998-588.

Griffin R. G. and L. H. Smith (1966). Experimental evaluation of outer case blowing or bleeding of a single stage axial flow compressor, part i—design of rotor blowing and bleeding configurations. *NASA Technical Paper* CR–54587.

Griffin R. G. and L. H. Smith (1970). Experimental evaluation of outer case blowing or bleeding of a single stage axial flow compressor, part vi—final report. *NASA Technical Paper* CR–54592.

Jichao L., J. Du, Z. Li and F. Ling (2018). Stability enhancement with self-recirculating injection in axial flow compressor. *Journal of Turbomachinery* 140(7), 071001.

Jichao L.，F. Lin，L. Liu，Z. Dong and C. Nie (2014). Experimental investigation of self-recirculating tip air injection in transonic axial flow compressor. *Journal of Mechanical Engineering* 50 （8）, 135-143.

Kenneth L. S., M. D. Hathaway, S. A. Thorp, A. J. Strazisar and M. B. Bright (2000). compressor stability enhancement using discrete tip injection. *ASME Journal of Turbomachinery* 123(1), 14-23.

Khaleghi, H. (2014). Effect of discrete endwall recirculation on the stability of a high-speed compressor rotor. *Aerospace Science and Technology* 37, 130-137.

Kumar, S., D. B. Alone, S. M. Thimmaiah, J. Mudipalli, L. Kumar, S. Jana, S. B. Kandagal and R. Ganguli (2022). Aeroelastic aspects of axial compressor stage with self-recirculating casing treatment. *Journal of Turbomachinery* 144(6), 061008.

Kumar, S., D. B. Alone, S. M. Thimmaiah, J. R. Mudipalli, L. Kumar, R. Ganguli, S. B. Kandagal (2021). Aerodynamic behavior of a transonic axial flow compressor stage with self-recirculating casing treatment. *Aerospace Science and Technology* 2021(230), 106587.

Kumar, S., R. J. Chotalia and S. Jana (2019). Single stage axial compressor stability management with self-recirculating casing treatment *AIAA Journal* 2019-0942.

Lonnie, R. and R. D. Moore (1978). Design and overall performance of four highly-loaded, high speed inlet stages for an advanced high pressure ratio core compressor. *NASA Technical Paper* TP-1337.

Nezym, V. Y. (2004). Development of new casing treatment configuration. *JSME International Journal Series B Fluids and Thermal Engineering* 47(4), 804-812.

Prince, D. C., D. C. Wisler and D. E. Hilvers (1974). Study of casing treatment stall margin improvement. *NASA* CR-134552.

Rabe, D. C. and C. Hah (2002). Application of Casing Circumferential Grooves for Improved Stall Margin in a Transonic Axial Compressor. In *ASME TURBO EPO*, Amsterdam, The Netherlands.

Wei, W., W. Chu and H. Zhang (2018). Mechanism study of performance enhancement in a subsonic axial flow compressor with recirculating casing treatment. *Proceedings of the Institution of Mechanical Engineers, Part G. Journal of Aerospace Engineering* 232(4), 680-693.

Weichert, S., I. Day and C. Freeman (2011). Self-regulating casing treatment for axial compressor stability enhancement. *ASME Paper* GT2011-4604.

Wenhao, L. (2020). *Mechanism Investigation of the Influence of Blade Angle Slot Casing Treatment*

on Axial Compressor Performance and Stability. M. D. thesis, the Northwestern Polytechnic University, Xi'an, China.

Wilke, I. and H. P. Kau (2002). A numerical investigation of the influence of casing treatments on the tip leakage flow in a HPC front stage. *ASME paper* GT-2002-30642.

Yang, H., D. Nuernberger, E. Nicke and A. Weber (2003). Numerical investigation of casing treatment mechanisms with a conservative mixed-cell approach. In *ASME Turbo Expo 2003, Collocated with the 2003 International Joint Power Generation Conference*, Atlanta, Georgia.

Zhang, H, D. Feiyang, W. Enhao, L. Wenhao and C. wuli (2022). Effect of different radial skewed angles of reversed blade-angle slot casing treatment on transonic axial flow compressor stability. *Proceedings of the Institution of Mechanical Engineers, Part G: Journal of Aerospace Engineering* 236(8), 1617-1632.

Zhang, H., L. Wenhao, C. Wuli and W. Enhao (2020). The effect of radial skew angles of blade angle slots on the stability and performance of an axial flow compressor. *In Turbo Expo: Power for Land, Sea, and Air,* American Society of Mechanical Engineers.

Zhang, H., A. Kang, C. Wuli, T. Feng and Z. Xudong (2018). Effects of blade-angle skewed slots on compressor performance. *Journal of Propulsion Technology* 39(06), 1260-1266.

Zhang, H., C. Wuli, W. Yanhui and S. Zhongliang (2010). Flow mechanisms of improving compressor performance through self-recirculation casing treatment. *Journal of Propulsion Technology* 2010(3), 8.

Zhang, H., C. Wuli, W. Yanhui, G. Peng and C. yuji (2009). Numerical investigation of the flow mechanisms of compressor stall delay through end wall self-recirculation. *Journal of Propulsion Technology* 30(002), 202-208.

Zhang, H., W. Jun, W. Yunpeng, C. Wuli and W. Yanhui (2016). Influence of the injecting position of self recirculation casing treatment on compressor performance. *Journal of Aerospace Power* 2016(5), 10.

Zhang, H., W. Yunpeng, W. Jun, C. Wuli and W. Yanhui (2015). Mechanism of improvement on axial-flow compressor stability with assembled casing treatment. *Journal of Aerospace Power* 30(1), 9.

Zhang, H., W. Yunpeng, W. Jun, C. Wuli, W. Yanhui and L. Xiangjun (2013). Full-annulus numerical investigation of axial flow compressor with self recirculation casing treatment. *Journal of Propulsion Technology* 34(7), 8.